Comparison of the properties of segregated layers in a bidispersed fluidized bed to those of a monodispersed fluidized bed

Yinuo Yao ⬤[*]

Department of Civil and Environmental Engineering, The Bob and Norma Street Environmental Fluid Mechanics Laboratory, Codiga Resource Recovery Center at Stanford, Stanford University, Stanford, California 94305, USA

Craig S. Criddle ⬤

Department of Civil and Environmental Engineering, Codiga Resource Recovery Center at Stanford, Stanford University, Stanford, California 94305, USA

Oliver B. Fringer ⬤

Department of Civil and Environmental Engineering, The Bob and Norma Street Environmental Fluid Mechanics Laboratory, Stanford University, Stanford, California 94305, USA

Since industrial fluidized-bed reactors typically operate with polydispersed particles, the ability to approximate such reactors as the superposition of corresponding monodispersed fluidized beds would greatly simplify their design and operation. To evaluate the validity of superposition of monodispersed reactor behavior, we evaluate the effects of bidispersity by comparing three-dimensional liquid-solid monodispersed and segregated bidipersed fluidized beds. Simulations were conducted using the immersed boundary method with direct forcing in a periodic domain and with particle Reynolds numbers of 20–70 based on the largest particle diameter. We show that the volume fraction, kinematic wave speed, particle velocity fluctuations, and collisional and hydrodynamic stresses in the segregated layers of a bidispersed fluidized bed can be well approximated by the corresponding properties of a monodispersed fluidized bed. In the transition region between the layers, only the volume fraction and collision stresses monotonically decrease with height. At low Reynolds numbers, particle velocity fluctuations in the upper layers are the largest. As the particle Reynolds number increases, particle velocity fluctuations in the transition and lower layers become the largest sequentially. At intermediate particle Reynolds numbers, the hydrodynamic stresses in the transition region are greater than those in the upper and lower layers. As the particle Reynolds number increases, the difference between the hydrodynamic stresses in the transition layer and the two layers become more significant. This paper demonstrates that, despite the clear segregation into layers that behave, such as monodispersed beds, the transition region is governed by complex bidispersed mechanisms that cannot be explained in terms of the particle behavior in the segregated layers. Overall, particle dynamics of the segregated layers in the bidispersed fluidized bed can be approximated with the corresponding monodispersed layers. The result implies that industrial applications, such as wastewater treatment performance in bidispersed or polydispersed fluidized beds can be predicted with results from past numerical or experimental studies of monodispersed fluidized beds.

---

[*]yaoyinuo@stanford.edu

I. INTRODUCTION

Liquid-solid fluidization is found in many industrial systems, such as wastewater treatment and chemical processes. In wastewater treatment, fluidized-bed reactors are widely used in treating both industrial and domestic wastewater [1–3]. Traditional biological domestic wastewater treatment is energy intensive [4], leading to the development of the Staged Anaerobic Fluidized-bed Membrane Bioreactor (SAF-MBR) that reduces energy demand in wastewater treatment by recovering energy in the form of methane [2,5,6]. In the SAF-MBR, wastewater is injected at the reactor bottom to fluidize granular activated carbon (GAC) which is used to support the growth of micro-organisms. Like many other fluidized beds, the nonuniformity of the GAC particles introduces more complexity in the fluidized-bed hydrodynamics. The ability to predict the hydrodynamics of fluidized beds used in wastewater treatment improves existing biological models for predicting and optimizing the treatment performance.

Since the monodispersed spherical fluidized bed is the most simplified and idealized fluidized-bed reactor, it has been studied extensively in the past [7–10]. Root-mean-square (rms) particle velocity fluctuations have been found to vary from 10% to 170% of the upflow velocity [8,10–12]. A series of papers focus on establishing a relationship between the upflow velocity and volume fraction. The most widely adopted relationship is based on the power-law model which can be applied to both fluidization and sedimentation and is given by

$$u^* = \frac{u_0}{w_{\text{ref}}} = k(1 - \phi)^n, \tag{1}$$

where u_0 is the superficial or upflow velocity of the fluidized bed, w_{ref} is the settling velocity of a single particle in the domain of interest, k is a constant to correct for high volume fractions [8,13–15], ϕ is the volume fraction, and n is the expansion or power-law exponent. Peak rms fluctuations have been shown to occur at a volume fraction of 30% [10]. At this volume fraction, the force on the particle transitions from collision to flow dominant [16].

Since monodispersed fluidized beds are not found in industrial applications, understanding the effects of polydispersity is critical. The ability to approximate polydispersed fluidized beds as the superposition of corresponding monodispersed fluidized beds would greatly simplify their design and operation by enabling application of existing understanding of monodispersed fluidized beds for which there is extensive literature [i.e., Eq. (1)]. A bidispersed liquid-solid fluidized bed represents a level of complexity that is sufficient to understand the basic effects of multiple particle sizes yet is not as computationally costly as a fully polydispersed system because particles with the smallest diameter dictate the grid resolution. Nevertheless, the number of parameters increases substantially in the study of a bidispersed bed. Because two interacting particles can have both different diameters and densities, the following three different cases are possible: (1) the same diameter but different density, (2) the same density but different diameter, and (3) different diameters and densities For cases (1) and (2), particle segregation generally occurs whereby the large (dense) particles sink to the bottom layer whereas the small (light) particles rise to the top layer. In a transition region between the two layers, both particles coexist but tend to move in opposite directions and the thickness of the transition region decreases with increasing particle diameter ratio or particle density ratio. Complete segregation is assumed to occur when the particle diameter ratio is greater than two [13]. The height of the bidispersed fluidized bed is typically assumed to be the sum of the heights of the two monodispersed fluidized-bed layers, and this has been shown to be quite accurate in sufficiently large systems [13,17]. Nevertheless, a large body of work has been devoted to developing models to predict the thickness of the transition region by solving the steady-state advection-diffusion equation in the axial z direction of the bed for particle $i = 1$ of 2,

$$-D_i \frac{\partial \phi_i}{\partial z} = \phi_i u_{\text{seg},i}, \tag{2}$$

where D_i is the dispersion coefficient, ϕ_i is the volume fraction, and $u_{\text{seg},i}$ is the segregation velocity [18–20]. These papers demonstrate that the volume fraction of the layers in a segregated

bidispersed fluidized bed can be approximated as a superposition of two monodispersed fluidized-bed layers. However, the dispersion coefficient and segregation velocity needed to predict the volume fraction are largely based on fitting and heuristics without quantification of the underlying particle microstructure physics. In this paper, we study these physics to obtain a more quantitative understanding of the processes affecting the transition region in a bidispersed fluidized bed.

To study the detailed hydrodynamics of a fluidized bed, there are both experimental and simulation approaches. In addition to the obvious advantage of studying real reactors without the need for models or simulations, the advantage of experiments is the ability to test a large number of different particle parameters in a relatively short period of time. This approach has been widely adopted to study macroscopic properties, such as modeling Re_t and n [7,21] and understanding the effect of particle properties on the collision pressure [22]. However, quantification of local hydrodynamics and microstructure in a fluidized bed with experiments is difficult [8], most notably because direct imaging of particles is only possible for dilute suspension [23,24]. In recent years, high-fidelity particle-resolved simulations (PRS) have gained popularity as a reliable technique to accurately resolve fluid-particle interactions. The approach is based on first principles and approximations are only needed to model particle collisions. With PRS, because individual particle information can be tracked over time, a more detailed examination of microstructure and local hydrodynamics in a fluidized bed is possible. Recently, the PRS approach has been widely adopted for a number of different problems, including extracting drag laws from arrays of particles [25–28] and understanding the detailed physics of flow-particle interactions in fluidized beds and particle suspensions [8–11,29–31].

In this paper, we present PRS results of liquid-solid monodispersed and segregated bidispersed fluidized-bed reactors to gain a detailed understanding of the effects of bidispersivity on the particle dynamics. A series of cases with different particle Reynolds numbers is studied, and the simulation results are used to validate the assumption of approximating segregated fluidized beds as the superposition of two monodispersed fluidized beds.

II. NUMERICAL METHODOLOGY AND SIMULATION SETUP

A. Equations and discretizations

The governing Navier-Stokes equations are solved in a three-dimensional rectangular domain containing an array of spherical particles. A source term $\mathbf{f}_{\text{IBM}}$, based on the direct-forcing IBM method is added to the incompressible Navier-Stokes equation to enforce no-slip boundary conditions on the particle surfaces as

$$\frac{\partial \boldsymbol{u}}{\partial t} + \boldsymbol{u} \cdot \boldsymbol{\nabla} \boldsymbol{u} = -\boldsymbol{\nabla} p + \nu_f \nabla^2 \boldsymbol{u} + \boldsymbol{f}_{\text{IBM}}, \tag{3}$$

subject to continuity, $\boldsymbol{\nabla} \cdot \boldsymbol{u} = 0$, where $\boldsymbol{u}$ is the velocity vector and p is the pressure normalized by the fluid density ρ_f. Equation (3) is solved on a uniform collocated Cartesian grid. Coupling between the momentum and the pressure equations is achieved using the fractional-step method proposed by Ref. [32]. The advection term is discretized with the explicit, three-step Runge-Kutta scheme described in Ref. [33]. The viscous term is discretized with the implicit Crank-Nicolson scheme to eliminate the associated stability constraint. The HYPRE library is used to solve the linear systems arising from the implicit discretization of the viscous terms and the pressure-Poisson equation [34,35]. To solve the interactions between the fluid and the particles, the direct forcing approach first proposed by Ref. [36] and improved by Ref. [37] is adopted. Collision models [38,39] are used to simulate particle-particle interactions when the separation distance between the particle surfaces is less than two grid cells. A detailed description and validation of the method can be found in Ref. [40].
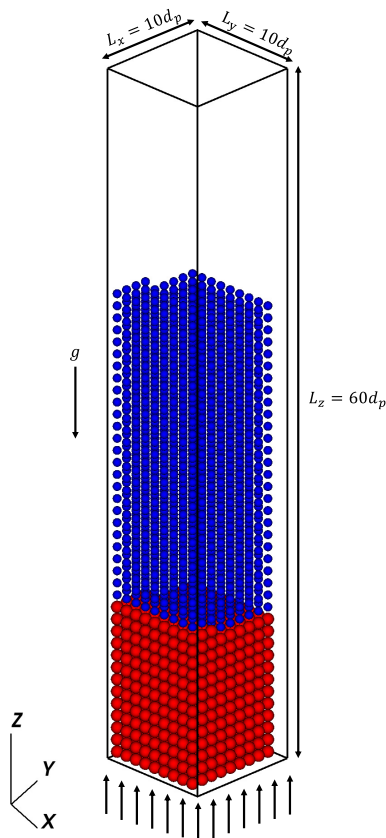
FIG. 1. The three-dimensional computational domain, showing the bidispersed fluidized bed and the uniform inflow velocity profile. Particle positions are initialized with $1d_{p,1}$ spacing for the simulation with $\mathrm{Re}_p = 40$ for FB-Bi-14.

B. Simulation setup

Three-dimensional simulations are conducted in the rectangular doubly periodic (x and y directions) domain shown in Fig. 1. The particles have a constant density $\rho_p = 1300 \text{ kg m}^{-3}$. Three different particle diameters $d_{p,1}$, $d_{p,2}$, and $d_{p,3}$ are chosen based on the monodispersed or bidispersed fluidized-bed configurations summarized in Table I. The fluid has density $\rho_f = 998.21 \text{ kg m}^{-3}$ and kinematic viscosity $\nu_f = 10^{-6} \text{ m}^2 \text{ s}^{-1}$. The Cartesian grid spacing is uniform and given by $\Delta x = \Delta y = \Delta z = h$ such that,

$$h = \frac{\max(d_{p,1}, d_{p,2}, d_{p,3})}{25.6} = \frac{\min(d_{p,1}, d_{p,2}, d_{p,3})}{18.3}, \tag{4}$$

which is sufficient to resolve the flow-particle interactions as demonstrated by various authors [36–38] and demonstrated with our code in Ref. [40]. The rectangular domain has a square cross section $L_x = L_y = 10d_{p,1}$ and a height $L_z = 60d_{p,1}$, giving a three-dimensional grid with $256 \times 256 \times 1536$ grid points. The time-step size Δt is calculated based on the advection and diffusion Courant number which are defined as $C_{\text{adv}} = u_0 \Delta t / h$ and $C_{\text{diff}} = \nu_f \Delta t / h^2$, respectively, and we ensure that $C_{\max} = \max(C_{\text{adv}}, C_{\text{diff}}) = 0.25$ for the case with the largest flow rate. In the simulations, the critical parameters are the particle diameter and the number of particles. Here, we choose the largest particle diameter $d_{p,1} = 0.002$ mm to compare the results to the monodispersed

TABLE I. Summary of number of particles used in the simulations. $N_{p,\text{mono}} = 2000$ is used for all monodispersed cases. $N_{p,d_{p,2}}$ and $N_{p,d_{p,3}}$ are calculated using Eq. (8) with respect to the upflow velocity. Particles with diameter $d_{p,1} = 2.0$ mm, $d_{p,2} = d_{p,1}/1.2$, and $d_{p,3} = d_{p,1}/1.4$ are used. Results from FB-Mono-10 were obtained from Ref. [16].

u_0 (m s^{-1})	FB-Mono-12 $N_{p,\text{mono}}$	FB-Bi-12 $N_{p,d_{p,1}}$	$N_{p,d_{p,2}}$	FB-Mono-14 $N_{p,\text{mono}}$	FB-Bi-14 $N_{p,d_{p,1}}$	$N_{p,d_{p,3}}$	FB-Mono-10 $N_{p,\text{mono}}$
0.010	2000	1000	1607	2000	1000	2376	2000
0.015	2000	1000	1565	2000	1000	2247	2000
0.020	2000	1000	1518	2000	1000	2106	2000
0.025	2000	1000	1465	2000	1000	1943	2000
0.030	2000	1000	1401	2000	1000	1749	2000
0.035	2000	1000	1321	2000	1000	2509	2000

simulations of Ref. [16], whereas $d_{p,2}$ and $d_{p,3}$ are calculated based on assuming

$$d_{p,1} = 1.2d_{p,2} = 1.4d_{p,3}. \tag{5}$$

The choice of the diameter ratio is designed to minimize the computational cost (that scales with the diameter ratio) whereas ensuring bidispersed behavior. For the monodispersed simulations, the number of particles $N_{p,\text{mono}} = 2000$ is used to ensure a sufficient fluidized bed height to obtain accurate statistics. For the bidispersed simulations, the number of particles $N_{p,bi}$ varies from case to case and is defined as

$$N_{p,bi} = N_{p,d_{p,1}} + N_{p,d_{p,j}}, \tag{6}$$

where $j = 2$ or 3, $N_{p,d_{p,1}}$ and $N_{p,d_{p,j}}$ are the number of particles with particle diameter $d_{p,1}$ and $d_{p,j}$, respectively. To ensure a fluidized-bed height that is sufficiently high to obtain good statistics, the bidispersed fluidized-bed height L_{bi} is kept the same as the monodispersed fluidized-bed height. Defining the monodispersed bed height determined by Ref. [16] as $L_{\text{mono},d_{p,1}}$, we require

$$L_{bi} = L_{\text{mono},d_{p,1}} = 2L_{bi,d_{p,j}} = 2L_{bi,d_{p,1}}. \tag{7}$$

Given $L_{\text{mono},d_{p,1}}$, $N_{p,\text{mono}}$, $d_{p,1}$, and $d_{p,j}$, if we assume the number of particles in the lower layer is $N_{p,d_{p,1}} = 1000$, then the number of particles in the upper layer is given by

$$N_{p,d_{p,j}} = \frac{L_x L_y L_{bi,d_{p,j}} \phi}{V_{p,d_{p,j}}}, \tag{8}$$

where $V_{p,d_{p,j}} = \pi d_{p,j}^3/6$ is the volume of a particle with diameter $d_{p,j}$ and ϕ can be estimated with Eq. (1). Table I summarizes the number of particles used in each simulation such that the largest number of particles used is $N_{p,bi} = 3376$. This represents a good balance between ensuring a sufficient fluidized bed height whereas minimizing the number of particles, which significantly increase the computational cost.

In this paper, in addition to the particle diameter ratio, the second parameter of interest is the particle Reynolds number. For a monodispersed fluidized bed, the particle Reynolds number is defined as $\text{Re}_{p,i} = u_0 d_{p,i}/\nu_f$ where $i = 1$, 2, or 3. For a bidispersed fluidized bed, two-particle Reynolds numbers $\text{Re}_{p,1}$ and $\text{Re}_{p,j}$ are defined based on the two-particle diameters $d_{p,1}$ and $d_{p,j}$ where $j = 2$ or 3. In order to maintain the same flow rate as the monodispersed simulations, we vary $\text{Re}_{p,1}$. In total, six simulations were conducted with 0.010 m s$^{-1} \leqslant u_0 \leqslant 0.035$ m s^{-1}, giving $20 \leqslant \text{Re}_{p,1} \leqslant 70$ for each configuration summarized in Table I, giving a total of 24 simulations. For all cases, the pressure is specified at the top boundary as $p = 0$, whereas a uniform inflow velocity of u_0 is specified at the bottom boundary.
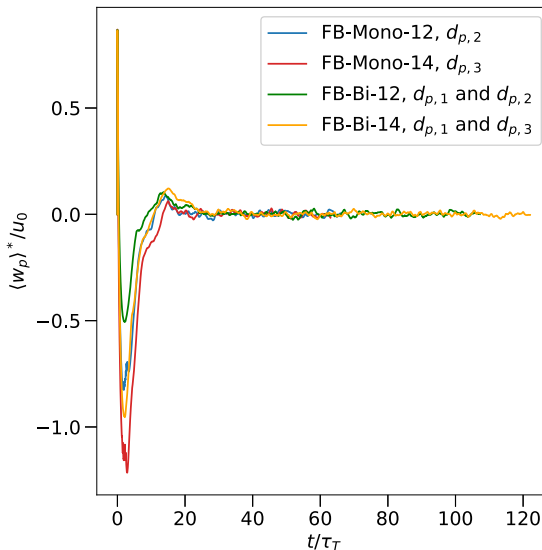
FIG. 2. Time series of the ensemble settling velocity $\langle w_p \rangle^*$ normalized by u_0 for $\mathrm{Re}_{p,1} = 40$ for all cases simulated except FB-Mono-10.

Simulations are initialized with a uniform array of particles, and the flow is started from rest. The upflow velocity leads to expansion of the bed and random motion of the particles until statistical equilibrium is reached at which time the dynamics are independent of the initial particle distribution and the total average drag force is in balance with the submerged weight of the particles. To understand the time evolution of particle variables and assess statistical equilibrium, we define the naive ensemble-average operator in which data for all particles are used as

$$\langle \{\cdot\} \rangle^* = \frac{1}{N_p} \sum_{n=1}^{N_p} \{\cdot\}_n, \tag{9}$$

where N_p is the total number of particles in the simulation and we monitor the ensemble-average vertical particle velocity $\langle w_p \rangle^*$. Here, we define a turnover time $\tau_T = d_{p,\max}/u_0$, and statistical equilibrium is achieved after $30\tau_T$ that is indicated by $\langle w_p \rangle^*$ fluctuating about zero. Figure 2 shows $\langle w_p \rangle^*$ as a function of maximum turnover time τ_T for different configurations with the same $\mathrm{Re}_{p,1} = 40$. The $\langle w_p \rangle^*$ of both monodispersed and bidispersed fluidized bed converges to zero, indicating statistical equilibrium. Here, we define the time-averaging operator,

$$\overline{\{\cdot\}} = \frac{1}{t_{\max} - t_i} \int_{t_i}^{t_{\max}} \{\cdot\} dt, \tag{10}$$

where $t_i = t_0 + 30\tau_T$ and t_0 is the spin-up time needed for the flow to reach statistical equilibrium.

III. RESULTS

A. Distribution of volume fraction in the bidispersed fluidized bed

Many researchers have reported that segregated bidispersed fluidized beds consist of three different regions (lower, transition, and upper layer) [13,19,20]. The volume fraction of the lower and upper layers can be approximated with the corresponding values for a monodispersed fluidized bed. To validate the volume fraction distribution of the segregated bidispersed fluidized bed, we compute the instantaneous Eulerian volume fraction $\phi(\boldsymbol{x}, t)$ following the procedure in Ref. [16]. We compute
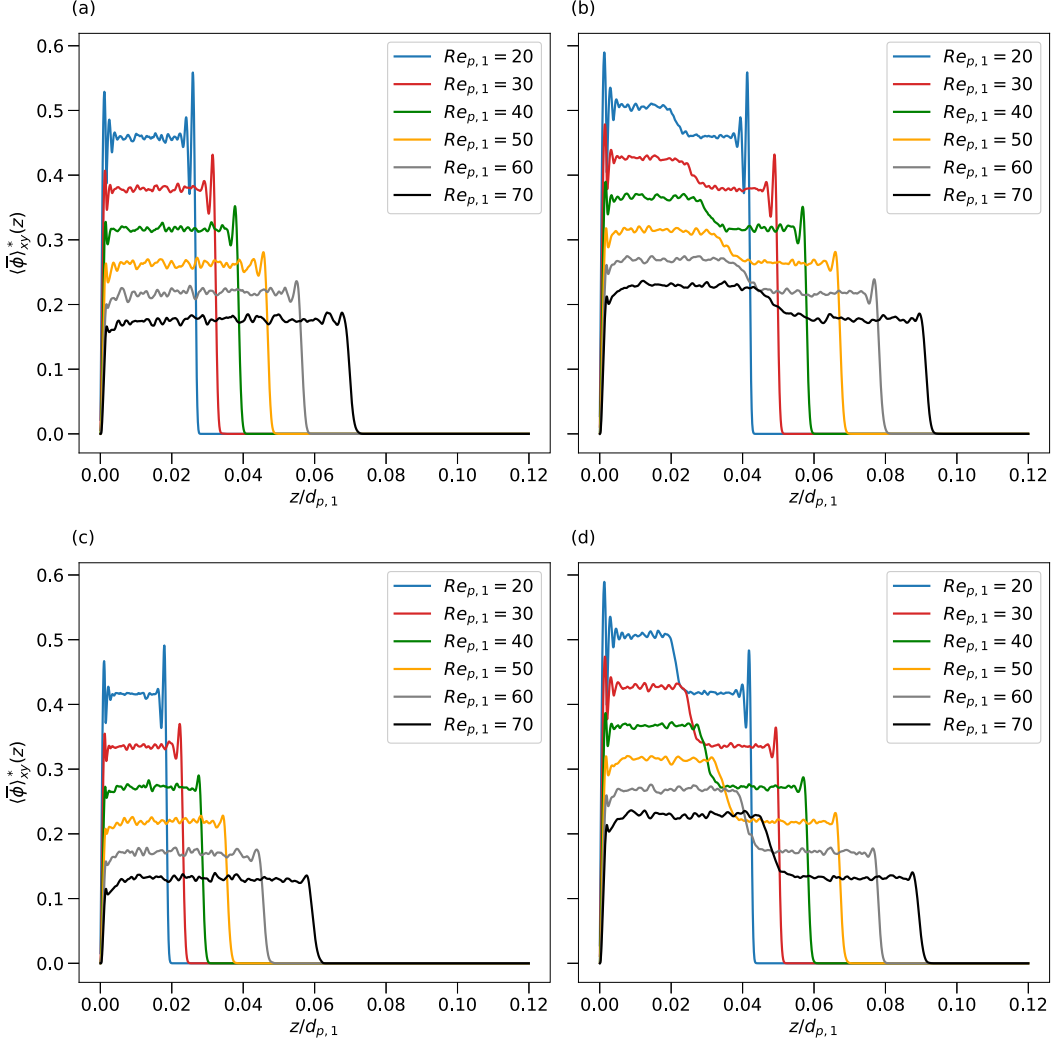
FIG. 3. Horizontally and time-averaged volume fraction $\langle\overline{\phi}\rangle^*_{xy}$ as a function of normalized vertical position $z/d_{p,1}$ for different particle Reynolds numbers $\text{Re}_{p,1}$. (a) FB-Mono-12. (b) FB-Bi-12. (c) FB-Mono-14. (d) FB-Bi-14.

the volume fraction as a function of vertical position by applying the Eulerian horizontal-averaging operator,

$$\langle\{\cdot\}\rangle^*_{xy} = \frac{1}{N_x N_y} \sum_{i,j=1}^{N_x N_y} \{\cdot\}_{ij}. \tag{11}$$

Figure 3 shows $\langle\overline{\phi}\rangle^*_{xy}(z)$ as a function of $z/d_{p,1}$ for different $\text{Re}_{p,1}$'s. Qualitatively, the $\langle\overline{\phi}\rangle^*_{xy}(z)$ of FB-Mono-12 and FB-Mono-14 approximately match the corresponding upper layers in FB-Bi-12 and FB-Bi-14. For quantitative comparison, we compute the vertically averaged (z) volume fraction $\langle\langle\overline{\phi}\rangle^*_{xy}\rangle_z$ by excluding the boundaries. To do so, we define a modified Eulerian vertical-averaging

operator,

$$\langle\{\cdot\}\rangle_z = \frac{1}{N_z^*} \sum_{k=z_b/h}^{z_t/h} \{\cdot\}_k, \tag{12}$$

where z_b and z_t are the bottom and top of the homogeneous fluidized-bed layers, respectively, and $N_z^* = (z_t - z_b)/h$ is the number of grid points in the z direction bounded by z_b and z_t. Homogeneous refers to the region of the fluidized bed that is not affected by the boundaries. In what follows, $\langle\langle\overline{\phi}\rangle_{xy}^*\rangle_z \equiv \langle\overline{\phi}\rangle$ will be assumed unless otherwise indicated.

For FB-Mono-12 and FB-Mono-14, we define z_b and z_t following the procedure in Ref. [16] by excluding the values near the top and bottom of the fluidized bed. For FB-Bi-12 and FB-Bi-14, the fluidized beds consist of three regions with a total of four boundaries (two for each segregated layer). In the transition region, the lower layer $\langle\overline{\phi}\rangle$ decreases monotonically from the lower to the upper layer $\langle\overline{\phi}\rangle$ as shown in Figs. 3(b) and 3(d). To define the boundaries of each region, we construct probability density functions (PDF) based on the particle vertical position with respect to particle diameter as

$$\mathbf{P}_\alpha(z) = \frac{1}{N_t} \sum_{t=1}^{N_t} \sum_{i=1}^{N_p} \left[\mathbf{1}_{z_l < z_{p,i}^t < z_u}\left(z_{p,i}^t\right) \right]\left[\mathbf{1}_{d_{p,i} = d_{p,j}}(d_{p,i}) \right], \tag{13}$$

where $z_{p,i}$ is the vertical position of the ith particle, z_l and z_u denote the lower and upper edges of the equally spaced bins having a width of $0.5d_{p,1}$, N_p is the total number of particles in the fluidized bed, $\mathbf{1}_{z_l < z_{p,i}^t < z_u}(z_{p,i}^t)$ is the indicator function,

$$\mathbf{1}_{z_l < z_{p,i}^t < z_u}\left(z_{p,i}^t\right) \begin{cases} 1, & z_l < z_{p,i}^t < z_u, \\ 0, & \text{otherwise}, \end{cases} \tag{14}$$

that determines whether particle i is located in the bin bounded by z_l and z_u, and $\mathbf{1}_{d_{p,i}=d_{p,j}}(d_{p,i})$ is the indicator function,

$$\mathbf{1}_{d_{p,i}=d_{p,j}}(d_{p,i}) \begin{cases} 1, & d_{p,i} = d_{p,j}, \\ 0, & \text{otherwise}, \end{cases} \tag{15}$$

to include particles with diameter $d_{p,j}$. Figure 4 shows the PDF of the particle vertical position for case FB-Bi-12 with $\mathrm{Re}_{p,1} = 40$. We define the top of the lower layer as

$$z_{t,\text{lower}} = \arg\min\left[\mathbf{P}_{d_{p,1}}(z)/\mathbf{P}_{d_{p,j}}(z) - \zeta_{\text{thresh}}\right], \tag{16}$$

and the bottom of the upper layer as

$$z_{b,\text{upper}} = \arg\min\left[\mathbf{P}_{d_{p,j}}(z)/\mathbf{P}_{d_{p,1}}(z) - \zeta_{\text{thresh}}\right], \tag{17}$$

where $\zeta_{\text{thresh}} = 100$ is an arbitrary threshold ratio to be set *a priori*. Large ζ_{thresh} will result in a more monodispersedlike segregated layer that leads to a larger transition region and smaller segregated region. Table II summarizes $z_{t,\text{lower}}$ and $z_{b,\text{upper}}$ for FB-Bi-12 and FB-Bi-14. With the boundaries defined in this way, we can compute $\langle\overline{\phi}\rangle$ for each segregated layer in cases FB-Bi-12 and FB-Bi-14.

Figure 5 shows the fit of $1 - \langle\overline{\phi}\rangle$ as a function of $\mathrm{Re}_{p,1}$ for different regions. Each bidispersed fluidized bed can fit two different lines for the upper and lower layers, resulting in a total of seven fitted lines (only three can be seen in the figure due to overlap). Overall, FB-Mono-12 [16] overlaps with the lower layer of FB-Bi-12 and FB-Bi-14 whereas FB-Mono-12 and FB-Mono-14 overlaps with the corresponding upper layer of FB-Bi-12 and FB-Bi-14. This shows that the volume fractions in the different layers of a segregated bidispersed fluidized bed can be approximated accurately with those of a monodispersed fluidized bed. Table III summarizes the fitted n that are closer to the predicted n by Ref. [21] and fitted k that is in the same range as reported by various authors [8,10]. Overall, n and k obtained from the monodispersed fluidized bed and corresponding layers in the bidispersed
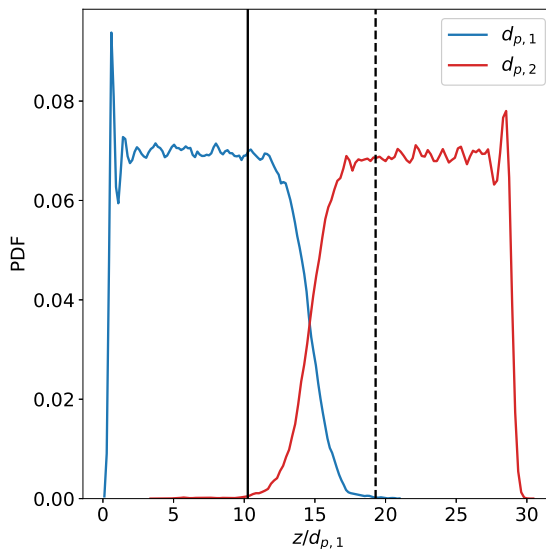
FIG. 4. PDF of particle vertical positions for the two-particle diameters in the case with $\text{Re}_{p,1} = 40$ for FB-Bi-12.

fluidized bed are indistinguishable, further demonstrating the accuracy of approximating the volume fraction in each segregated layer as that in a monodispersed layer without boundary effects.

B. Kinematic wave speed

In the previous section, the fluidized bed is characterized by the volume fraction and the particle Reynolds number. However, the volume fraction fluctuates about a mean value which exhibits alternating regions of low and high volume fractions, resulting in waves [41–43]. Comparison between the wave speed of segregated bidispersed and monodispersed fluidized beds will further validate the assumption of approximating segregated bidispersed fluidized beds as a superposition of two monodispersed fluidized beds.

Based on the classification of fluidization by Refs. [41,42], the cases simulated in this paper are classified as unstable fluidization that is characterized by persistent particle velocity fluctuations. Figure 14(a) shows a typical volume fraction fluctuation $\phi' = \langle \overline{\phi} \rangle_{xy} - \langle \overline{\phi} \rangle$ plot in two-dimensional space-time. Qualitatively, propagating waves are indicated by regions of porosity that are periodic

TABLE II. Summary of the top boundary of lower layer $z_{t,\text{lower}}$ and the bottom boundary of upper layer $z_{b,\text{upper}}$ in the bidispersed fluidized bed. The transition region is defined as the difference between $z_{t,\text{lower}}$ and $z_{b,\text{upper}}$.

	FB-Bi-12		FB-Bi-14	
u_0 (m s^{-1})	$z_{t,\text{lower}}/d_{p,1}$	$z_{b,\text{upper}}/d_{p,1}$	$z_{t,\text{lower}}/d_{p,1}$	$z_{b,\text{upper}}/d_{p,1}$
0.010	8.44	12.7	9.35	25.9
0.015	8.74	16.3	11.2	22.0
0.020	11.5	17.5	12.7	19.3
0.025	13.3	22.0	14.5	16.6
0.030	15.4	23.8	17.2	14.2
0.035	18.4	27.7	20.5	11.8
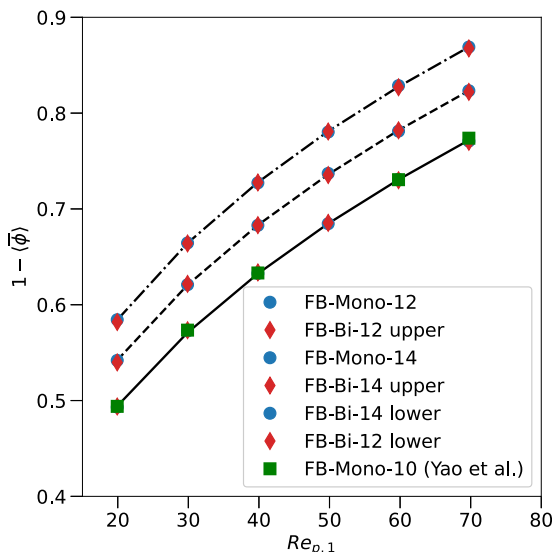
FIG. 5. Porosity $1 - \langle \overline{\phi} \rangle$ as a function of $\text{Re}_{p,1}$ for the simulated monodispersed and bidispersed cases. The lines were constructed based on fitting to the power-law equation (1).

in space and time. However, due to the random noise, extracting wave speeds from Fig. 14(a) is difficult. In Appendix B, wave speeds estimated with three different approaches are compared, namely, (1) naive, (2) two-dimensional autocorrelation, and (3) the dispersion relationship. The results indicate that the autocorrelation approach is the most accurate and is adopted in this paper.

Reference [44] relates volume fraction to wave speed with

$$c = kn\phi(1 - \phi)^{n-1}w_{\text{ref}}, \tag{18}$$

where c is the wave speed and other variables are consistent with Eq. (1). Figures 6(a)–6(c) show the wave speeds computed with different particle diameters using the autocorrelation approach and model [Eq. (18)]. Overall, the computed wave speeds are very similar to the wave speeds computed with the model. Interestingly, the wave speed in the different layers in the FB-Bi-12 and FB-Bi-14 cases agree with the corresponding monodispersed fluidized-bed cases even though the boundary conditions on each segregated layer in cases FB-Bi-12 and FB-Bi-14 are different. For illustration, case FB-Mono-12 is prescribed with a uniform inflow profile whereas the upper layer of case FB-Bi-12 is subjected to the nonuniform flow at the transition region. This shows that the wave speed is controlled by the particle properties and local porosity rather than the inflow.

TABLE III. Summary of fitted n and k with respect to each monodispersed fluidized bed and segregated layers in the bidispersed fluidized bed. All coefficients of determination R^2 for these fits are 1. n_{zaki} and n_{ga} are calculated using Refs. [7,21] respectively.

Parameters	$d_{p,1}$			$d_{p,2}$		$d_{p,3}$	
	FB-Mono-10	FB-Bi-12	FB-Bi-14	FB-Mono-12	FB-Bi-12	FB-Mono-14	FB-Bi-14
n	2.81	2.83	2.81	3.00	2.99	3.15	3.14
k	0.71	0.72	0.72	0.74	0.74	0.76	0.76
n_{ga}		2.89			2.95		3.02
n_{zaki}		2.61			2.71		2.80
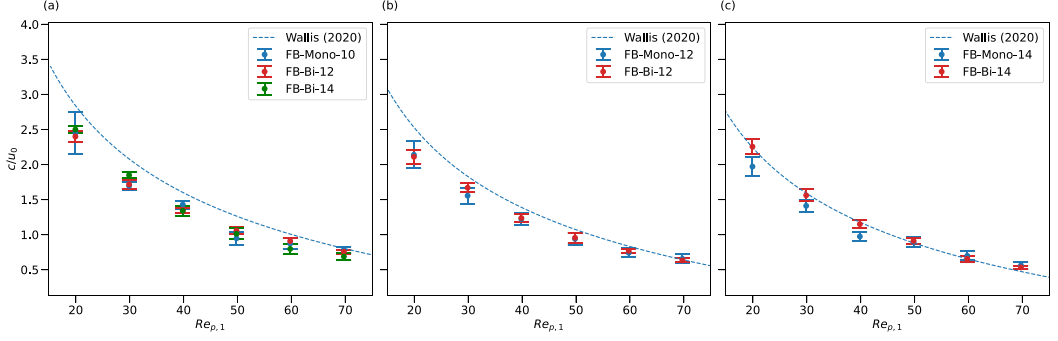
FIG. 6. Wave speed based on the autocorrelation as a function of $\mathrm{Re}_{p,1}$ for (a) $d_{p,1}$, (b) $d_{p,2}$, and (c) $d_{p,3}$.

C. Velocity fluctuations

To understand the effect of particle velocity fluctuations in a segregated bidispersed fluidized bed, we compute the root-mean-square velocity,

$$u_{\mathrm{rms},\alpha} = \overline{\sqrt{\langle u'_\alpha u'_\alpha \rangle}}, \tag{19}$$

where $u'_\alpha = u_\alpha - \langle \overline{u} \rangle_\alpha$ is the particle velocity fluctuation and $\alpha = x$, y or z. In a suspended particle system, Ref. [23] discovered that particle velocity fluctuations depend on the domain size for $\min(L_x, L_y, L_b) < 10 d_{p,\max} \phi^{-1/3}$ and otherwise scale as $2w_t \phi^{1/3}$. By simulating Stokes sedimentation, Ref. [45] demonstrated that the dependence on the domain size exists with periodic horizontal and nonperiodic z-direction boundaries. Figure 7 shows the particle velocity fluctuations u'_α for case FB-Mono-12 as a function of the normalized bed height for $\mathrm{Re}_{p,1} = 30$ and 60. Particle velocity fluctuations initially increase at a higher rate as L_b increases. When L_b is sufficiently large (above the black line), the increase in particle velocity fluctuations is less significant. Since the heights of the segregated layers in cases FB-Bi-12 and FB-Bi-14 are less than the critical height $10 d_{p,\max} \phi^{-1/3}$, they differ from the height of the corresponding monodispersed fluidized bed. Therefore, particle
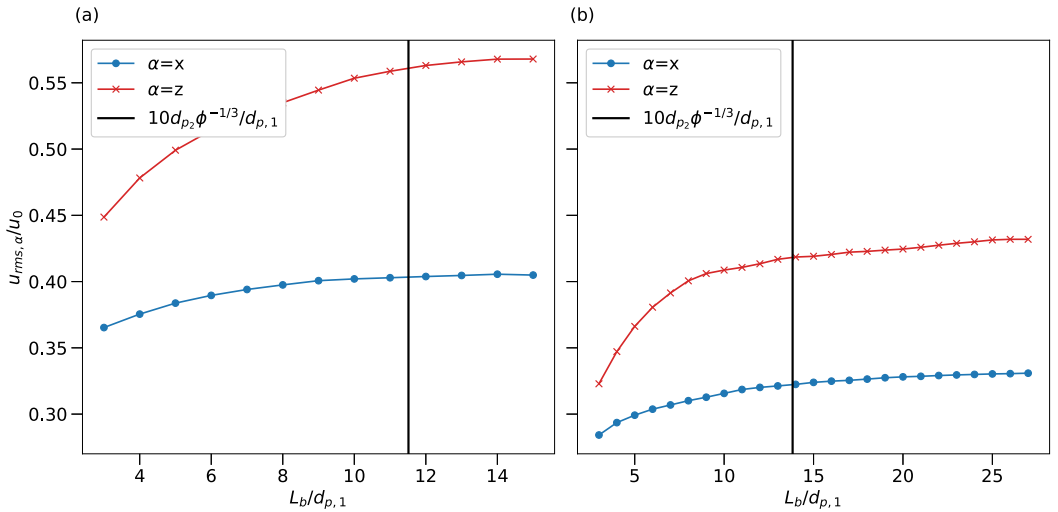
FIG. 7. Particle velocity fluctuations as a function of the fluidized-bed height L_b for case FB-Mono-12 with (a) $\mathrm{Re}_{p,1} = 30$ and (b) $\mathrm{Re}_{p,1} = 60$.
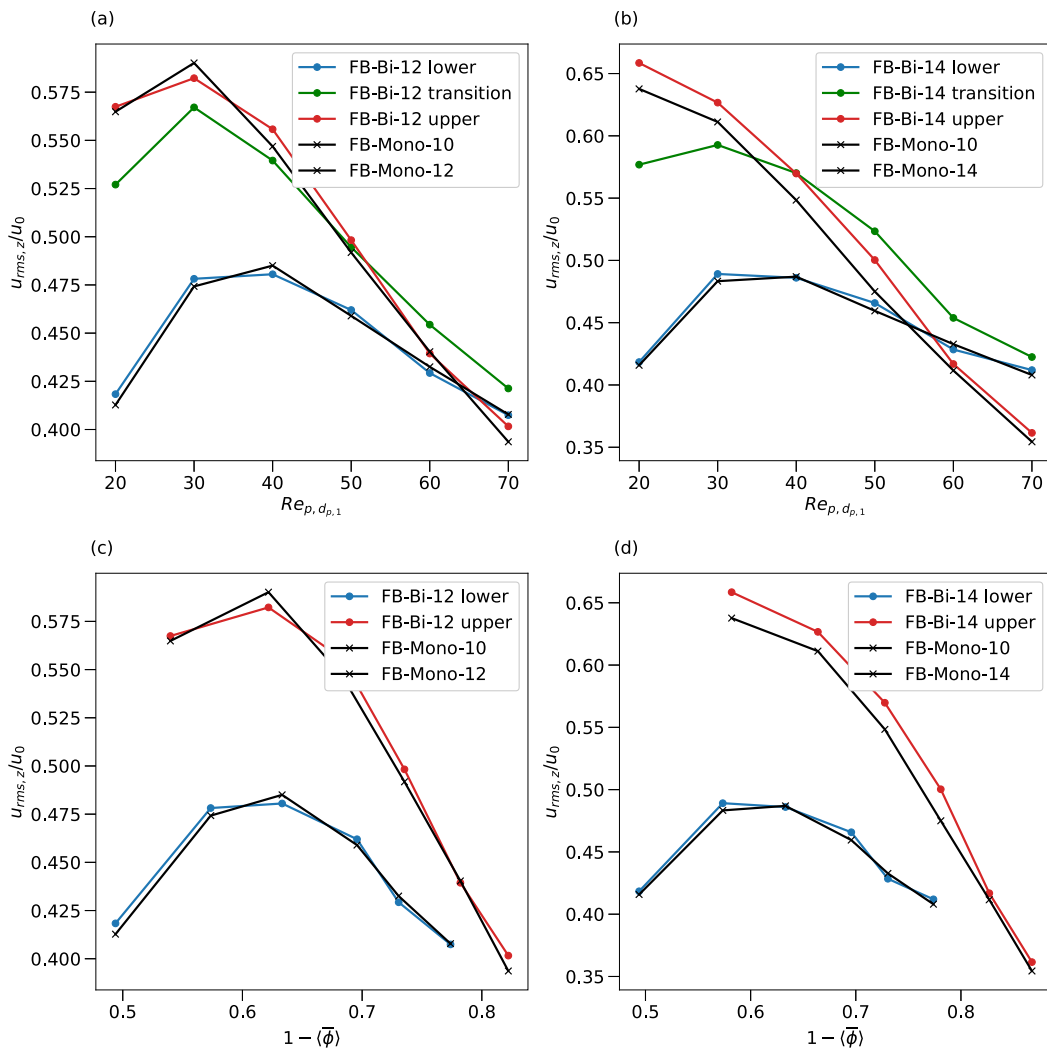
FIG. 8. Normalized particle velocity fluctuations as a function of $\mathrm{Re}_{p,1}$ for (a) $d_{p,1}/d_{p,2} = 1.2$ and $d_{p,1}/d_{p,3} = 1.4$ and $1 - \langle \overline{\phi} \rangle$ for (c) $d_{p,1}/d_{p,2} = 1.2$ and (d) $d_{p,1}/d_{p,3} = 1.4$.

velocity fluctuations in the monodispersed fluidized bed are calculated with particles located below the desired height to eliminate the effect of L_b on particle velocity fluctuations. Figures 8(a) and 8(b) show the normalized particle velocity fluctuations as a function of $\mathrm{Re}_{p,1}$. With the same bed height, the normalized particle velocity fluctuations for cases FB-Mono-10, FB-Mono-12, and FB-Mono-14 are nearly identical to those of the corresponding layers in the bidispersed fluidized-bed cases. At low Reynolds numbers ($\mathrm{Re}_{p,1} \leqslant 40$), the upper segregated layer has the largest normalized particle velocity fluctuations, followed by the transition and lower layers. As the Reynolds number increases, particle velocity fluctuations in the transition layer become greater than those of the upper segregated layer. For $\mathrm{Re}_{p,d_{p,1}} > 60$, the particle velocity fluctuations in the transition layer are the highest, followed by the lower and upper layers. The trends in Fig. 8 indicate that the normalized particle velocity fluctuations of the lower layers will eventually become the largest. This observation is due to the different particle properties and volume fraction operating at a common $\mathrm{Re}_{p,1}$, resulting in different porosity due to different particle properties. To eliminate this effect, Figs. 8(c) and

8(d) show the normalized particle velocity fluctuations as a function of the porosity $1 - \langle \overline{\phi} \rangle$. The normalized particle velocity fluctuations are expected to be zero for both a single-particle ($\phi \approx 0$) and a packed bed ($\phi \approx 0.6$), resulting in a maximum value at an intermediate porosity. The upper segregated layer has consistently higher normalized particle velocity fluctuations than the lower segregated layer at the same porosity due to the decreasing particle cluster lifespan with increasing Archimedes number [40], which is defined as

$$\text{Ar} = \frac{g(s-1)d_{p,i}^3}{\nu_f^2}, \tag{20}$$

where $i = 1$, 2 or 3, $d_{p,i}$ is the diameter of particle i, g is the gravitational acceleration, and $s = \rho_p / \rho_f$ is the particle-fluid density ratio. According to Ref. [40], particles are more likely to form long-lived clusters for particles with lower Ar due to ineffective collisions that are unlikely to break particle clusters formed by wake entrainment. With more long-lived clusters, particles experience appreciable acceleration as a cluster resulting in more significant normalized particle velocity fluctuations. Despite higher particle velocity fluctuations for lower Ar, we would like to point out that Fig. 8 resembles more realistic fluidized-bed operation. With a common upflow velocity, particles with different Ar's cannot be operated at the same porosity. To optimize reactor mixing that is likely to coincide with the peak in particle velocity fluctuations [16], both layers must be considered separately.

D. Autocorrelation and self-diffusivity

In this section, we compute the integral timescale and self-diffusivity for different regions in the bidispersed fluidized bed and compare them to the corresponding monodispersed fluidized bed. As defined by Refs. [9,10,46], the autocorrelation function is given by

$$R_{\alpha\alpha}(\tau) = \frac{\langle u'_\alpha(t_0) u'_\alpha(t_0 + \tau) \rangle}{\langle [u'_\alpha(t_0)]^2 \rangle}, \tag{21}$$

where τ is the given time lag and $\alpha = x$, y, or z. Following the procedure to quantify the errors in computing the integral timescale due to finite simulation time in Ref. [16], we compute the approximate integral timescale as

$$\mathbb{E}(\mathcal{T}_{\alpha,\text{cal}}) = \frac{1}{N_\tau - N_{\tau,\text{thresh}}} \sum_{i=N_{\tau,\text{thresh}}}^{N_\tau} \mathcal{T}_{\alpha,\text{cal}}^i, \tag{22}$$

$$\text{STD.}(\mathcal{T}_{\alpha,\text{cal}}) = \sqrt{\mathbb{E}(\mathcal{T}_{\alpha,\text{cal}}^2) - \mathbb{E}(\mathcal{T}_{\alpha,\text{cal}})^2}, \tag{23}$$

where $N_\tau = t/\tau_T$ and $N_{\tau,\text{thresh}}$ is the threshold time needed to reach statistical equilibrium and the calculated integral timescale with N_τ is defined as

$$\mathcal{T}_{\alpha,\text{cal}}^{N_\tau} = \int_0^{t_f} R_{\alpha\alpha}(\tau) d\tau. \tag{24}$$

Figure 9(a) shows the effects of N_τ on the computed integral timescale for the entire fluidized bed. For each respective fluidized-bed height, $\mathcal{T}_{\alpha,\text{cal}}$ initially increases as N_τ increases and fluctuates about a mean value after $N_\tau \approx 10$, demonstrating that the computed integral timescale has converged in time. The fluctuations are likely due to the presence of waves in the fluidized bed which produce alternating positive and negative autocorrelations [9,16]. We also compute $\mathcal{T}_{\alpha,\text{cal}}$ as a function of L_b by considering particles that are located in the desired range of the fluidized bed for 99% of the simulated duration. As shown in Fig. 9(b), $\mathbb{E}(\mathcal{T}_{\alpha,\text{cal}})$ converges as $L_b/d_{p,1}$ increases. After $L_b > L_{b,\text{crit}}$, the integral timescale is independent of the fluidized-bed height. Since $L_b < L_{b,\text{crit}}$ for cases FB-Bi-12 and FB-Bi-14, we adopt a similar approach as Sec. III C by computing a reduced L_b for the monodispersed simulations (cases FB-Mono-12 and FB-Mono-14). As shown in Fig. 10, the
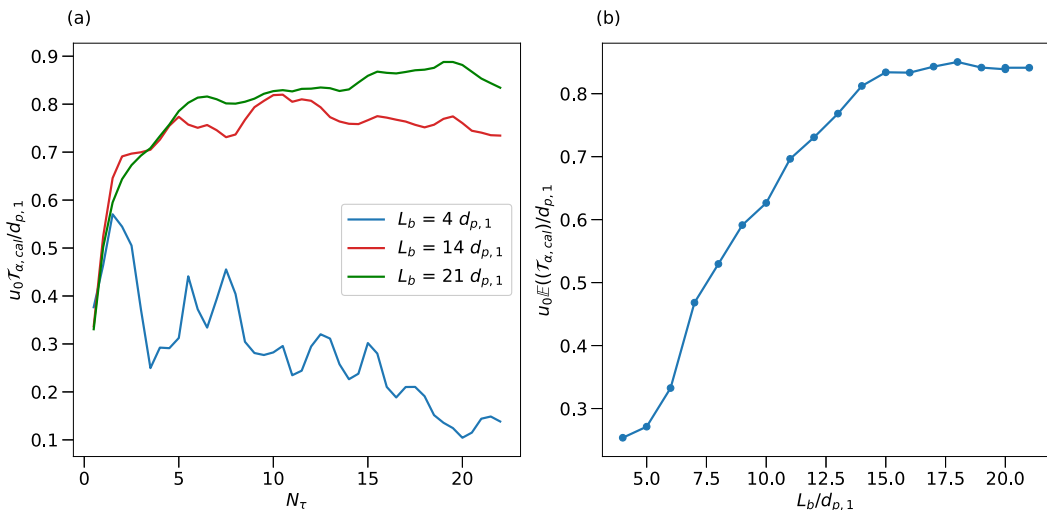
FIG. 9. Calculated integral timescale as a function of (a) simulated duration N_τ and (b) fluidized-bed height $L_b/d_{p,1}$ for case FB-Mono-12 with $\mathrm{Re}_{p,1} = 40$.

integral timescale for the bidispersed cases are on the same order of magnitude as the truncated monodispersed integral timescales. The nonmonotonic behavior is due to the error associated with $L_b < L_{b,\mathrm{crit}}$. Since the main focus is not on the absolute magnitude but on the relative magnitude between the monodispersed and bidispersed fluidized beds, approximating the segregated layers in bidispersed fluidized beds with corresponding monodispersed fluidized beds is still valid.

Following Refs. [9,46], the self-diffusivity is defined as

$$\mathcal{D}_{\alpha,\mathrm{cal}}^{N_\tau} = \int_0^{t_f} R_{\alpha\alpha}(\tau)\langle[u_\alpha'(t_0)]^2\rangle d\tau. \tag{25}$$

Similar to the integral timescale, the self-diffusivity initially depends on L_b until $L_b > L_{b,\mathrm{crit}}$ (not shown). Therefore, to compare to the bidispersed cases, we compute the truncated self-diffusivity
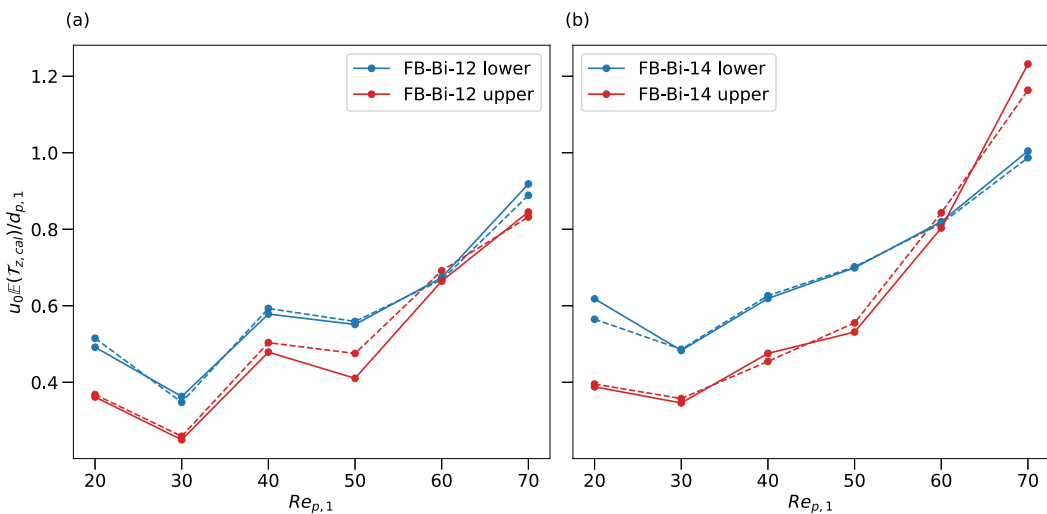
FIG. 10. Expected integral timescale as a function of $\mathrm{Re}_{p,1}$ for (a) $d_{p,1}/d_{p,2} = 1.2$ and $d_{p,1}/d_{p,3} = 1.4$.
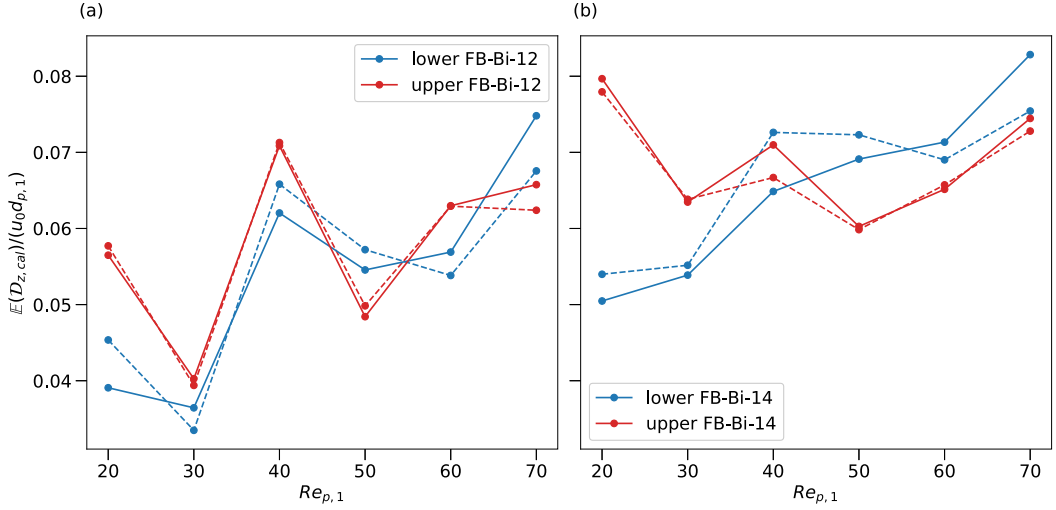
FIG. 11. Self-diffusivity as a function of $\mathrm{Re}_{p,1}$ for (a) $d_{p,1}/d_{p,2} = 1.2$ and (b) $d_{p,1}/d_{p,3} = 1.4$.

for the monodispersed cases. Figure 11 shows that the self-diffusivity of the bidispersed cases is comparable to the self-diffusivity of the monodispersed cases, indicating the validity of characterizing bidispersed fluidized beds using properties of the corresponding monodispersed layers.

E. Particle-particle and fluid-particle interactions

Reference [16] showed that the dominant mechanism inducing particle velocity fluctuations shifts from collisions to hydrodynamic forces as the particle Reynolds number increases. Following the approach outlined in Ref. [16], we compute the normal contact stress σ_{col}, normal lubrication stress σ_{lub} and hydrodynamic stresses σ_{hydro} in the bidispersed fluidized bed. Figure 12 shows
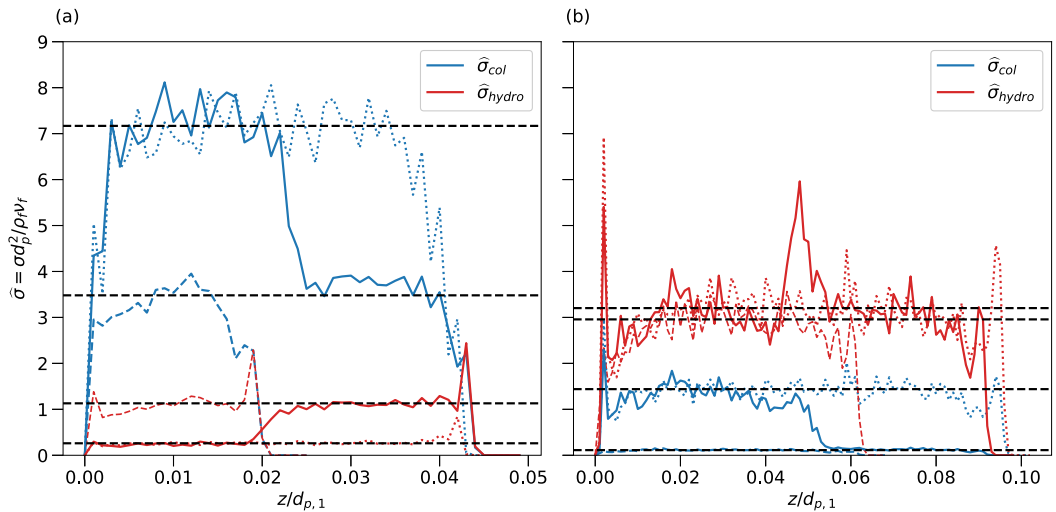
FIG. 12. Normal contact stress and hydrodynamic stress as a function of vertical position for $d_{p,1}/d_{p,3} = 1.40$ and with (a) $\mathrm{Re}_{1,p} = 20$ and (b) $\mathrm{Re}_{1,p} = 70$. Solid lines correspond to bidispersed fluidized-bed layers, and dotted lines correspond to monodispersed layers.

the magnitude of each stress as a function of vertical position for $\mathrm{Re}_{p,1} = 20$ and 70 for cases FB-Bi-14, FB-Mono-10 and FB-Mono-14. For the range of Reynolds number simulated, lubrication stresses are negligible (not shown). At low Reynolds numbers for the bidispersed simulation, the normal contact stress smoothly transitions from a high value in the lower layer to a lower value in the upper layer because of the reduced likelihood of collisions in the higher-porosity upper layer. The collision stresses in the upper and lower layers are roughly equal to the stresses in the corresponding monodispersed cases, and the hydrodynamic stresses are negligible due to the low upflow velocity. At high Reynolds numbers, similar trends are observed in which the normal contact stress decreases monotonically to zero moving from the lower to the upper layers. Unlike the collision stress, however, the hydrodynamic stress peaks in the transition region rather than monotonically decreasing from the lower to the upper layers. In the transition region at higher Reynolds numbers, more vigorous velocity fluctuations are induced when large particles coexist with small particles because small particles are strongly affected by the wakes of the large particles, thus, leading to a peak in the hydrodynamic stress in the transition region.

Figure 13 shows that the collision stresses decrease monotonically from the lower to the upper layers for all cases, indicating a strong dependence of the collision stress on the Archimedes number in each layer. In addition, the collision stresses in the lower and upper layers of the bidispersed fluidized-bed match those of the corresponding monodispersed fluidized bed. This shows that collision stresses in the bidispersed fluidized bed can be approximated as those in the monodispersed fluidized bed. However, because the hydrodynamic stress is a weaker function of the Archimedes number in each layer but a strong function of particle Reynolds number, the hydrodynamic stresses in the transition region are greater than those in the lower and upper layers in the bidispersed fluidized bed. Nevertheless, this analysis demonstrates that both collision and hydrodynamic stresses in the lower and upper layers of a segregated bidispersed fluidized bed can be approximated by the corresponding values in a monodispersed fluidized bed.

IV. CONCLUSION

We utilized PRS to compare the effects of the particle Reynolds number and bidispersity on both macroscopic and microscopic behavior of a fluidized bed in a three-dimensional domain. The particle Reynolds number was varied by varying the flow rate suspending particles in the axial direction. Analysis of various statistics provided detailed comparison between monodispersed and bidispersed fluidized beds. We have validated the assumption in approximating the volume fraction of segregated bidispersed fluidized bed with the volume fraction of two corresponding monodispersed fluidized beds. Fitting the porosity $1 - \langle \overline{\phi} \rangle$ to $\mathrm{Re}_{p,1}$ further confirms that each segregated layer in the bidispersed fluidized bed behaves like a monodispersed fluidized bed and can be calculated using a power-law relationship. To understand the effects of wave speed in the monodispersed and bidispersed fluidized beds, we filter out random noise in the volume fraction fluctuation using a low-pass filter and approximate the wave speed using three different approaches. As compared to the corresponding monodispersed fluidized bed with uniform inflow conditions, the upper layer of a bidispersed fluidized bed has an equivalent nonuniform flow conditions due to the transition layer. For a inflow-dominated wave speed, the wave speed of the upper layer of the bidispersed fluidized bed is expected to differ from that of the corresponding monodispersed fluidized bed. Results show that the nonuniform flow that fluidizes the upper layer of a bidispersed fluidized bed does not result in a different wave speed. This reveals that the wave speed is instead controlled by the local porosity rather than the inflow conditions. As the fluid flows through the voids between particles, inflow conditions are no longer important in determining the wave speed of the volume fraction fluctuations. Within the computed uncertainty bounds, the wave speed in each layer in the bidispersed fluidized bed agrees with the wave speed in the corresponding monodispersed fluidized bed.

Examination of particle velocity fluctuations shows that they are a strong function of the fluidized-bed height until the fluidized-bed height is greater than the critical bed height $10 d_p \phi^{-1/3}$.
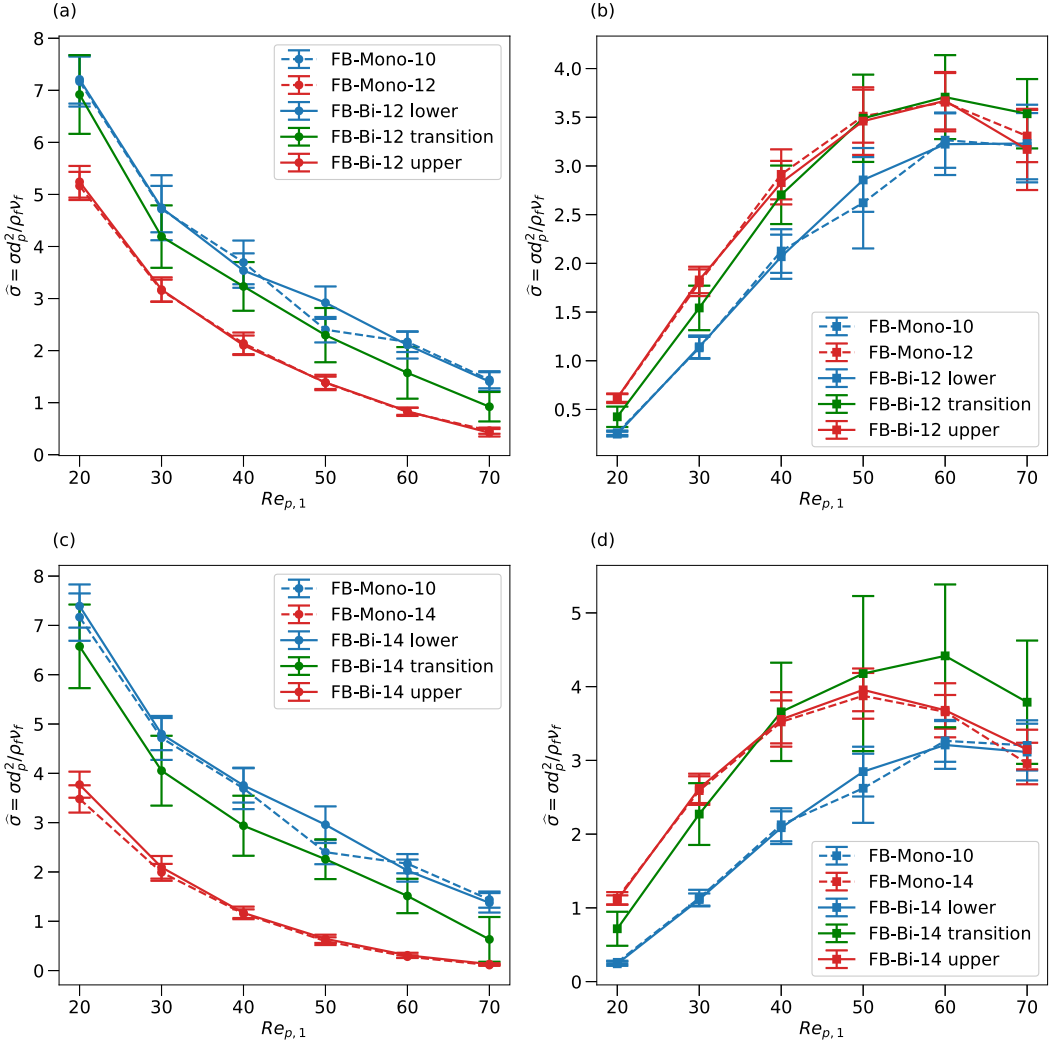
FIG. 13. The computed normal contact stress and hydrodynamic stress as a function Reynolds number $Re_{p,1}$. (a) Normal contact stress for $d_{p,1}/d_{p,2} = 1.2$. (b) Hydrodynamic stress for $d_{p,1}/d_{p,2} = 1.2$. (a) Normal contact stress for $d_{p,1}/d_{p,3} = 1.4$. (a) Hydrodynamic stress for $d_{p,1}/d_{p,3} = 1.4$.

Due to limitations related to computational cost, the heights of the lower and upper layers of the bidispersed fluidized bed are less than the critical bed height. Therefore, we compute the particle velocity fluctuations of the monodispersed fluidized beds with bed heights equivalent to the corresponding upper and lower layers of the bidispersed fluidized beds. By computing particle velocity fluctuations in the monodispersed fluidized bed with equivalent heights, we have shown that the particle velocity fluctuations in the bidispersed fluidized bed match those of the corresponding monodispersed fluidized bed. Similarly, the convergence of the integral timescales and self-diffusivity are affected by both the fluidized-bed height and simulated duration until a critical bed height and sufficient long simulated duration are attained. Results show that the simulated duration of both the monodispersed and bidispersed fluidized beds is sufficient. However, the bed heights of the upper and lower layers are insufficient to obtain converged statistics. In order to compare with the corresponding monodispersed fluidized beds, we compute the integral timescale

of the monodispersed fluidized beds with an equivalent bed height to the corresponding upper and lower layers in the bidispersed fluidized beds. Using this approach, we confirmed that both self-diffusivity and integral timescales in the bidispersed fluidized bed can be approximated by their corresponding values for a monodispersed fluidized bed.

By quantifying the lubrication, collision, and hydrodynamic stresses, we showed that collision stresses are a strong function of both Archimedes number and particle Reynolds number, while hydrodynamic stresses depend more strongly on the particle Reynolds number. Furthermore, the collision stress in the bidispersed fluidized bed decreases monotonically from the lower to the upper layer whereas the hydrodynamic stress has a peak in the transition region at a high Reynolds number. This points out the need to develop models that can accurately capture this observations. Nevertheless, the magnitude of collision and hydrodynamic stresses in the segregated layers of the bidispersed fluidized bed are very similar to those in the corresponding monodispersed fluidized bed.

The results clearly indicate that both macroscopic and microscopic properties of a monodispersed fluidized bed can be transferred to a segregated bidispersed liquid-solid fluidized bed. However, in the transition region, whereas the volume fraction and collision stresses are always bounded by values in the lower and upper layers, the particle velocity fluctuations and hydrodynamic stresses are not always monotonically decreasing with height. This shows that the properties of the transition region cannot be approximated as simple averages of those properties in the segregated layers.

APPENDIX A: SIMULATION SETUP OF A FLUIDIZED BED

For the simulation of FB-Mono-10 [16], three-dimensional simulations are conducted with $N_p = 2000$ particles in a rectangular domain. The particles have an Archimedes number Ar = 23 600. The grid spacing is uniform in the x, y, and z directions, and the grid resolution is given by $\Delta x = \Delta y = \Delta z = h = d_p/25.6$. The rectangular domain has cross-sectional dimension $L_x = L_y = 10d_p$, and its length is $L_z = 60d_p$ with $256 \times 256 \times 1536$ grid points. The time-step size is $\Delta t = 1.5 \times 10^{-4}$ s, resulting in a maximum advection Courant number of 0.5 for the six cases simulated. The cases are run with periodicity in the x and y directions. The pressure is specified at the top boundary as $p = 0$, whereas at the bottom boundary the inflow velocity is specified as uniform and given by
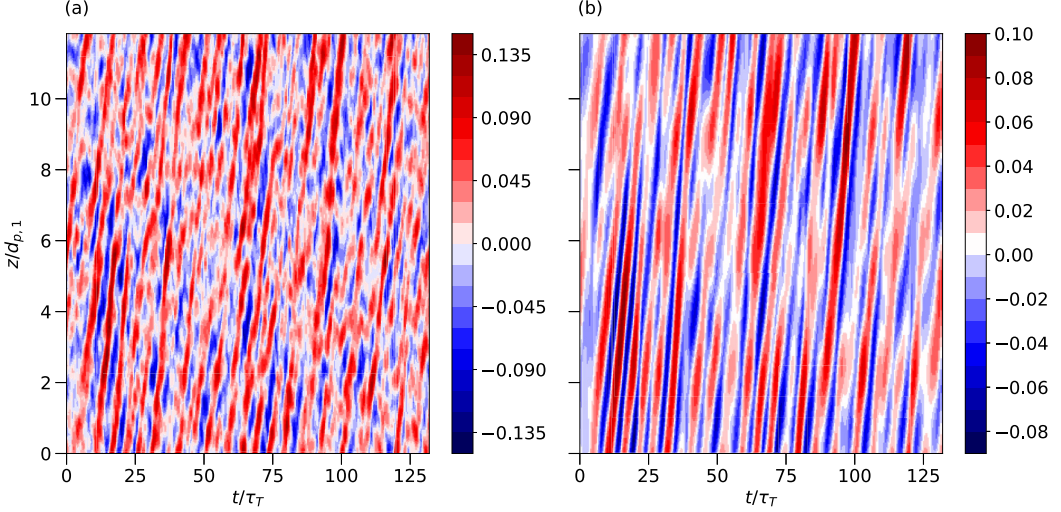
FIG. 14. Volume fraction fluctuation ϕ' as a function of time t and vertical position z at $\mathrm{Re}_p = 60$ in the lower layer for case FB-Bi-12. (a) Unfiltered ϕ', (b) reconstructed low-pass filtered ϕ'.

$\widetilde{U}$. The primary parameter of interest is the particle Reynolds-number $\mathrm{Re}_{p,1} = u_0 d_{p,1}/\nu_f$ where the average upflow velocity at the inlet u_0 is varied to investigate Reynolds-number effects. A total of six simulations were conducted with $0.010 \leqslant u_0 \leqslant 0.035$, giving $20 \leqslant \mathrm{Re}_{p,1} \leqslant 70$.

APPENDIX B: EVALUATION OF DIFFERENT APPROACHES IN COMPUTING WAVE SPEED

In this Appendix, we compare three different approaches which are as follows: (1) naive, (2) autocorrelation, and (3) dispersion relation in computing wave speed from volume fraction. To separate the wave motion from the random noise, we followed the procedure by Ref. [16] to reconstruct $\phi(z, t)$ into its low $\phi_{k < k_{\mathrm{thresh}}}(z, t)$ and high $\phi_{k \geqslant k_{\mathrm{thresh}}}(z, t)$ wave-number components using Fourier transforms with cutoff wave-number k_{thresh}. In this paper, $k_{\mathrm{thresh}} = L_b/d_{p,1}$, where L_b is the height of the monodispersed layer or each segregated layer in the bidispersed fluidized bed. Figure 14(b) shows the reconstructed low wave-number $\phi_{k < k_{\mathrm{thresh}}}(z, t)$ signal. Compared to Fig. 14(a), the wavelike behavior is more distinct, and an approximate wave speed can be computed based on the slope of the features on the z-t plane.

For the naive approach, we approximate the wave speed directly from Fig. 14(b) by computing the average of z/t for t that results in the top five largest $\phi_{k < k_{\mathrm{thresh}}}(z, t)$'s for each respective z. The naive approach wave-speed c_{na} is formally defined as

$$c_{na} = \frac{1}{N_k N_i} \sum_{k=1}^{N_k} \sum_{i=1}^{N_i} \frac{z_k}{t_{k,i}}, \tag{B1}$$

where $N_i = 5$ is a constant that determines the number of values to be used for each z, N_k is the number of grid points in the fluidized bed, z_k is the vertical position, and t_k is the value of t that results in the top-N_i largest $\phi_{k < k_{\mathrm{thresh}}}(z, t)$ at z_k which is defined as

$$t_k = \underset{\psi \in \phi_{k < k_{\mathrm{thresh}}}(z,t), |\psi|=N_i}{\arg \max} \sum_{v \in \psi} v, \tag{B2}$$

where $|\psi|$ denotes the number of elements in ψ.

For the two-dimensional autocorrelation approach, we followed the procedure in Ref. [43]. The space-time autocorrelation of ϕ' is defined as $\langle \phi'(z + \Delta z, t + \Delta t) \rangle$. By assuming
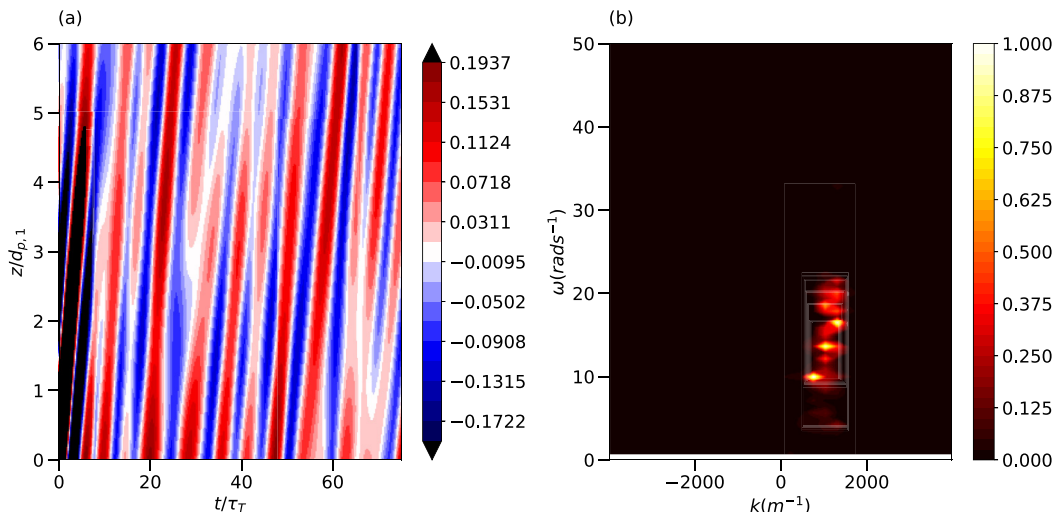
FIG. 15. (a) Autocorrelation of the low-pass filtered volume fraction fluctuation ϕ' as a function of time t and vertical position z and (b) energy spectra of the reconstructed volume fraction fluctuation ϕ' as a function of wave-number k and frequency ω at $\mathrm{Re}_p = 60$ in the lower layer for case FB-Bi-12.

$\phi'(z, t) = \phi'(z - ct)$ in the form of a propagating wave and wave-speed $c = \Delta z / \Delta t$, the autocorrelation of ϕ' is reduced to $(\phi')^2(z, t)$, appearing as the maximum value in the autocorrelation plot. The advantage of this approach is that the dominant wave will be amplified, hence, making the wave-speed approximation more reliable. A detailed validation of this approach can be found in Ref. [43]. Figure 15(a) shows a typical space-time autocorrelation plot of ϕ'. Although the wavelike behavior is clearer when compared to Fig. 14(b), the wavelike bands in our simulations are not as clear as those in Ref. [43]. A plausible explanation for this lack of obvious wavelike motion is the method of forcing in our simulations. In Ref. [43], a triply periodic domain is used, and vertical forcing is added directly to the flow to balance the weight of particles. Our simulations are doubly periodic with inflow and outflow specified at the top and bottom boundaries, thus, representing a more realistic and perhaps noisier result characterized by disturbances propagating through the domain due to boundary effects. To approximate the autocorrelation wave-speed c_{auto}, Eq. (B1) is used by computing the ratio of z to t.

For the dispersion relationship approach, we construct the energy spectra of ϕ' using the Fourier transform to compare the energy spectra as a function of frequency ω and wave-number k and then approximate the wave speed with $c = \omega/k$. Figure 15(b) shows the energy spectra normalized by the maximum value in two-dimensional k-ω space. (A peak is defined where the normalized energy spectrum is greater than 0.8, and each peak represents a wave-speed ω/k). As shown in Fig. 15(a), three peaks are observed that fall on the same line defined by $\omega = c_{FT} k$, indicating the dominance of three different wave modes propagating at the same speed. The wave-speed c_{FT} is approximated by fitting the line defined by $\omega = c_{FT} k$ to the three peaks.

Figure 16 shows the wave speed computed with different approaches for FB-Mono-12. Overall, the wave speed derived from the autocorrelation function has the least uncertainty, indicated by the smallest standard deviation. The naive approach gives results with similar averages but much larger standard deviations. This is expected because of ineffective noise suppression as shown in Fig. 14(b). Interestingly, the dispersion relationship approach gives almost identical results as the autocorrelation approach. However, the main disadvantage of the dispersion relationship is the need for a large domain. If the domain is small such that the wavelength of the wave is greater than the fluidized-bed height, smeared peaks will be observed leading to inaccurate results. Since the segregated bed height in cases FB-Bi-12 and FB-Bi-14 are smaller than the wavelength, the
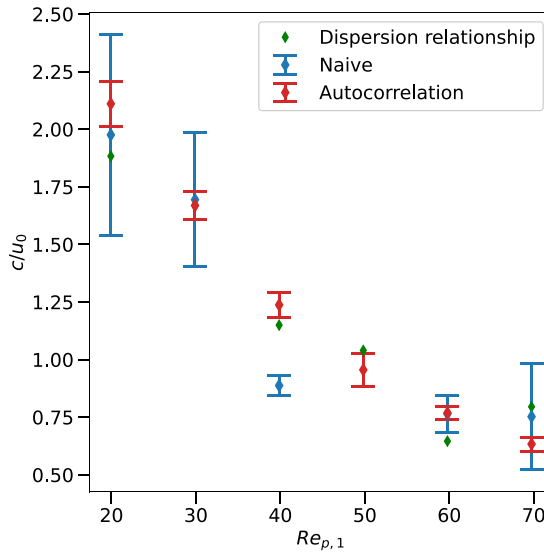
FIG. 16. Wave speed derived from different approaches as a function of $Re_{p,1}$ for case FB-Mono-12.

dispersion relationship is less accurate for these cases. In the remainder of this paper, we adopt the autocorrelation approach to compare wave speeds.

[1] C. Shin and J. Bae, Current status of the pilot-scale anaerobic membrane bioreactor treatments of domestic wastewaters: A critical review, Bioresour. Technol. **247**, 1038 (2018).

[2] C. Shin, P. L. McCarty, J. Kim, and J. Bae, Pilot-scale temperate-climate treatment of domestic wastewater with a staged anaerobic fluidized membrane bioreactor (SAF-MBR), Bioresour. Technol. **159**, 95 (2014).

[3] P. L. McCarty, J. Kim, C. Shin, P.-H. Lee, and J. Bae, Anaerobic fluidized bed membrane bioreactors for the treatment of domestic wastewater, in *Anaerobic Biotechnology* (Imperial College Press, London, 2015), pp. 211–242.

[4] Y. D. Scherson, S.-G. Woo, and C. S. Criddle, Production of nitrous oxide from anaerobic digester centrate and its use as a co-oxidant of biogas to enhance energy recovery, Environ. Sci. Technol. **48**, 5612 (2014).

[5] C. Shin, E. Lee, P. L. McCarty, and J. Bae, Effects of influent DO/COD ratio on the performance of an anaerobic fluidized bed reactor fed low-strength synthetic wastewater, Bioresour. Technol. **102**, 9860 (2011).

[6] C. Shin, J. Bae, and P. L. McCarty, Lower operational limits to volatile fatty acid degradation with dilute wastewaters in an anaerobic fluidized bed reactor, Bioresour. Technol. **109**, 13 (2012).

[7] J. F. Richardson and W. N. Zaki, Sedimentation and fluidisation: Part I, Trans. Inst. Chem. Eng. **32**, 35 (1954).

[8] X. Yin and D. L. Koch, Hindered settling velocity and microstructure in suspensions of solid spheres with moderate reynolds numbers, Phys. Fluids **19**, 093302 (2007).

[9] A. Esteghamatian, A. Hammouti, M. Lance, and A. Wachs, Particle resolved simulations of liquid/solid and gas/solid fluidized beds, Phys. Fluids **29**, 033302 (2017).

[10] D. P. Willen and A. Prosperetti, Resolved simulations of sedimenting suspensions of spheres, Phys. Rev. Fluids **4**, 014304 (2019).

[11] A. A. Zaidi, T. Tsuji, and T. Tanaka, Hindered settling velocity & structure formation during particle settling by direct numerical simulation, Proc. Eng. **102**, 1656 (2015).

[12] A. Hamid, J. J. Molina, and R. Yamamoto, Direct numerical simulations of sedimenting spherical particles at non-zero reynolds number, RSC Adv. **4**, 53681 (2014).

[13] R. Di Felice, Hydrodynamics of liquid fluidisation, Chem. Eng. Sci. **50**, 1213 (1995).

[14] R. Di Felice, The sedimentation velocity of dilute suspensions of nearly monosized spheres, Int. J. Multiphase Flow **25**, 559 (1999).

[15] R. Di Felice and E. Parodi, Wall effects on the sedimentation velocity of suspensions in viscous flow, AIChE J. **42**, 927 (1996).

[16] Y. Yao, C. S. Criddle, and O. B. Fringer, Competing flow and collision effects in a monodispersed liquid-solid fluidized bed, arXiv:2106.06140.

[17] N. Epstein, B. P. Leclair, and B. B. Pruden, Liquid fluidization of binary particle mixtures-i: Overall bed expansion, Chem. Eng. Sci. **36**, 1803 (1981).

[18] S. C. Kennedy and R. H. Bretton, Axial dispersion of spheres fluidized with liquids, AIChE J. **12**, 24 (1966).

[19] M. S. Khan, G. M. Evans, A. V. Nguyen, and S. Mitra, Analysis of particle dispersion coefficient in solid-liquid fluidised beds, Powder Technol. **365**, 60 (2020).

[20] K. P. Galvin, R. Swann, and W. F. Ramirez, Segregation and dispersion of a binary system of particles in a fluidized bed, AIChE J. **52**, 3401 (2006).

[21] J. Garside and M. R. Al-Dibouni, Velocity-Voidage relationships for fluidization and sedimentation in Solid-Liquid systems, Ind. Eng. Chem. Proc. Des. Dev. **16**, 206 (1977).

[22] R. Zenit, M. L. Hunt, and C. E. Brennen, Collisional particle pressure measurements in solid-liquid flows, J. Fluid Mech. **353**, 261 (1997).

[23] P. N. Segré, E. Herbolzheimer, and P. M. Chaikin, Long-Range Correlations in Sedimentation, Phys. Rev. Lett. **79**, 2574 (1997).

[24] X. Lei, B. J. Ackerson, and P. Tong, Settling Statistics of Hard Sphere Particles, Phys. Rev. Lett. **86**, 3300 (2001).

[25] S. Tenneti, R. Garg, and S. Subramaniam, Drag law for monodisperse gas-solid systems using particle-resolved direct numerical simulation of flow past fixed assemblies of spheres, Int. J. Multiphase Flow **37**, 1072 (2011).

[26] G. Akiki, W. C. Moore, and S. Balachandar, Pairwise-interaction extended point-particle model for particle-laden flows, J. Comput. Phys. **351**, 329 (2017).

[27] Y. Tang, E. A. J. F. Peters, J. A. M. Kuipers, S. H. L. Kriebitzsch, and M. A. van der Hoef, A new drag correlation from fully resolved simulations of flow past monodisperse static arrays of spheres, AIChE J. **61**, 688 (2015).

[28] R. Beetstra, M. A. van der Hoef, and J. A. M. Kuipers, Numerical study of segregation using a new drag force correlation for polydisperse systems derived from lattice-boltzmann simulations, Chem. Eng. Sci. **62**, 246 (2007).

[29] S. H. L. Kriebitzsch, M. A. van der Hoef, and J. A. M. Kuipers, Fully resolved simulation of a gas-fluidized bed: A critical test of DEM models, Chem. Eng. Sci. **91**, 1 (2013).

[30] A. Ozel, J. C. Brändle de Motta, M. Abbas, P. Fede, O. Masbernat, S. Vincent, J.-L. Estivalezes, and O. Simonin, Particle resolved direct numerical simulation of a liquid-solid fluidized bed: Comparison with experimental data, Int. J. Multiphase Flow **89**, 228 (2017).

[31] M. Uhlmann and T. Doychev, Sedimentation of a dilute suspension of rigid spheres at intermediate galileo numbers: the effect of clustering upon the particle motion, J. Fluid Mech. **752**, 310 (2014).

[32] Y. Zang, R. L. Street, and J. R. Koseff, A non-staggered grid, fractional step method for Time-Dependent incompressible Navier-Stokes equations in curvilinear coordinates, J. Comput. Phys. **114**, 18 (1994).

[33] M. Rai and P. Moin, Direct simulations of turbulent flow using finite-difference schemes, J. Comput. Phys. **96**, 15 (1991).

[34] R. D. Falgout and U. M. Yang, hypre: A library of high performance preconditioners, in *Computational Science—ICCS 2002*, edited by P. M. A. Sloot, A. G. Hoekstra, C. J. Kenneth Tan, and J. J. Dongarra (Springer, Berlin/Heidelberg, 2002), pp. 632–641.

[35] E. Chow, A. J. Cleary, and R. D. Falgout, Design of the hypre preconditioner library, in *SIAM Workshop on Object Oriented Methods for Inter-Operable Scientific and Engineering Computing* (SIAM, Philadelphia, 1998).

[36] M. Uhlmann, An immersed boundary method with direct forcing for the simulation of particulate flows, J. Comput. Phys. **209**, 448 (2005).

[37] T. Kempe and J. Fröhlich, An improved immersed boundary method with direct forcing for the simulation of particle laden flows, J. Comput. Phys. **231**, 3663 (2012).

[38] E. Biegert, B. Vowinckel, and E. Meiburg, A collision model for grain-resolving simulations of flows over dense, mobile, polydisperse granular sediment beds, J. Comput. Phys. **340**, 105 (2017).

[39] T. Kempe and J. Fröhlich, Collision modelling for the interface-resolved simulation of spherical particles in viscous fluids, J. Fluid Mech. **709**, 445 (2012).

[40] Y. Yao, C. S. Criddle, and O. B. Fringer, The effects of particle clustering on hindered settling in high-concentration particle suspensions, J. Fluid Mech. **920**, A40-1 (2021).

[41] J. J. Derksen and S. Sundaresan, Direct numerical simulations of dense suspensions: wave instabilities in liquid-fluidized beds, J. Fluid Mech. **587**, 303 (2007).

[42] P. Duru, M. Nicolas, J. Hinch, and Ã. Guazzelli, Constitutive laws in liquid-fluidized beds, J. Fluid Mech. **452**, 371 (2002).

[43] D. P. Willen, A. J. Sierakowski, G. Zhou, and A. Prosperetti, Continuity waves in resolved-particle simulations of fluidized beds, Phys. Rev. Fluids **2**, 114305 (2017).

[44] G. B. Wallis, *One-Dimensional Two-Phase Flow* (Courier, New York, 2020).

[45] N.-Q. Nguyen and A. J. C. Ladd, Microstructure in a settling suspension of hard spheres, Phys. Rev. E **69**, 050401(R) (2004).

[46] H. Nicolai, B. Herzhaft, E. J. Hinch, L. Oger, and E. Guazzelli, Particle velocity fluctuations and hydrodynamic self-diffusion of sedimenting non-brownian spheres, Phys. Fluids **7**, 12 (1995).